Earth Planet. Sci. Lett. 669 (2025) 119577

Contents lists available at ScienceDirect

Earth and Planetary Science Letters

journal homepage: www.elsevier.com/locate/epsl

# A high attenuation layer around 1000 km depth

Shuyang Sun *, Yanick Ricard, Stéphanie Durand, Eric Debayle

*Université Lyon 1, ENS de Lyon, CNRS, LGL-TPE, Villeurbanne, F-69622, France*

ARTICLE INFO

Editor: H. Thybo

*Keywords:*
Seismic attenuation
Mantle structure
Body-waves

ABSTRACT

We build a 1D model of body wave shear attenuation ($Q_{L1D}$) using various S-phase measurements, including direct (S, SS, SSS, SSSS), core-reflected (ScS, ScSScS, ScSScSScS), diffracted ($S_{diff}$) and their depth phases (e.g., sS, sScS, $sS_{diff}$), providing extensive depth and spatial coverage. We process 15 years of more than 400,000 seismic data recorded down to a high quality database of 40,000 records. Differential anelastic delay times are measured using the instantaneous frequency matching method between observations and synthetics computed in the 3D mantle model S40RTS and crust model CRUST1.0 using SPECFEM, fully accounting for the 3D velocity heterogeneities. The average differential anelastic time delays for all S phases remain consistently negative across all epicentral distances suggesting that Earth mantle is less attenuating than the PREM model and can be approximated by scaling the PREM quality factor by 1.2. However, S, SS, SSS, SSSS and their depth phases consistently exhibit a high-attenuation (low $Q_\mu$) anomaly when the seismic waves travel around 1000 km depth. This feature is confirmed in $Q_{L1D}$ model obtained from 1D inversion. The high attenuation zone highlights the peculiar nature of the mantle around 1000 km depth, which is potentially linked to a global low-viscosity layer, suggesting plume accumulation beneath the upper-lower mantle boundary. We also confirm the existence of the high-attenuation zone in the asthenosphere, indicating the uppermost part of the upper and lower mantles have a similar structure: an attenuating layer beneath a more elastic shell. A low-attenuation zone is also observed near 1900 km depth.

## 1. Introduction

In the Earth, the mathematical abstraction of an average radial model for seismic velocity and density is fairly obvious since the seismic velocity and density are mostly functions of the radius with weak lateral variations (at most 10% and most often around 1% (Dziewonski, 1984; Kennett and Engdahl, 1991; Montagner and Kennett, 1996)). The Earth is not purely elastic, and energy dissipation occurs as seismic waves travel through the Earth's interior. This dissipation is measured in terms of quality factor $Q$, where $Q^{-1}$ quantifies the attenuation of seismic waves as the loss of elastic energy per cycle. There is bulk attenuation $Q_\kappa^{-1}$ and shear attenuation $Q_\mu^{-1}$, but $Q_\kappa$ is expected to be much larger than $Q_\mu$ (see e.g., Romanowicz and Mitchell, 2007). Attenuation often varies exponentially with temperature, material grainsize, composition (Karato, 2007; Lekić et al., 2009; Faul and Jackson, 2015) and can exhibit large lateral variations, making the concept of average model more questionable. Radial reference models, including attenuation, remain however indispensable for calculating synthetic seismograms. They also supply a backbone for a very large number of mineralogical, geochemical or geodynamic researches comparing seismic data with laboratory experiments (Mattern et al., 2005; Stixrude and Lithgow-Bertelloni, 2005) or using radial model to define reservoirs (e.g., Zindler and Hart, 1986) or mechanical stratification (Ricard et al., 1993).

However, measuring seismic attenuation is challenging even to simply propose a 1D model. The average $Q_\mu$ model used in PREM, is mostly obtained from normal mode observations that constrain the average values and from surface waves that essentially define the shallow structure of the lithosphere and asthenosphere. Several radial models of $Q_\mu$ quality factor based on body waves have been published, but they significantly disagree (e.g. Lawrence and Wysession, 2006; Hwang and Ritsema, 2011; Durand et al., 2013; Zhu et al., 2022). Body waves are used to constrain $Q_\mu$ by observing the anelastic delay times $\delta t^*$ of seismic phases (Bhattacharyya et al., 1996). This can be done by measuring the wave amplitudes in the time domain (e.g., Chan and Der, 1988; Chaves and Ritsema, 2016; Zhang et al., 2019) or in the frequency domain (e.g., Sipkin and Revenaugh, 1994; Suetsugu, 2001; Hwang and Ritsema, 2011; Zhu et al., 2022). It can also be done by measuring the angular phases of the seismic pulses instead of their amplitudes

* Corresponding author.
*E-mail address:* sysungeo@outlook.com (S. Sun).

https://doi.org/10.1016/j.epsl.2025.119577
Received 12 May 2025; Received in revised form 3 August 2025; Accepted 5 August 2025

Available online 19 August 2025

(Matheney and Nowack, 1995), as will be discussed in the following. Measuring body wave attenuation is however challenging, as evidenced by the abnormally large variations in $\delta t^*$ measurements (Reid et al., 2001; Hwang and Ritsema, 2011; Durand et al., 2013). These variations are due to the effects of radiation pattern, crust, phase interference, scattering and focusing/defocusing which need an accurate 3D velocity model to be taken into account (Zhou, 2009; Ruan and Zhou, 2012).

In this study, we propose to mitigate these effects by using, as references, seismograms that have been computed in a 3D elastic Earth's mantle. We have measured differential anelastic time delays $\delta t^*$ between observed and synthetic S phases for a massive body-wave dataset. In total, we have analyzed seismograms recorded at $\approx 2100$ global seismic stations for $\approx 350$ deep and shallow earthquakes between 2009 and 2023. To maximize the depth and spatial coverage, we included several S phases including S, $S_2$, $S_3$, $S_4$, ScS, $ScS_2$, $ScS_3$, $S_{diff}$, and their depth counterparts (i.e., sS, $sS_2$...). With this huge data set, we build a 1D $Q_\mu(z)$ model, $Q_{L1D}$. As we only work with S waves, we obtain $Q_\mu$ models since the quality factor $Q_\kappa$ that only affects the P waves cannot be assessed by our measurements.

## 2. Instantaneous phase measurement

The attenuation measurements can be done in the time domain or in the frequency domain. Here, we adopt the Instantaneous Frequency Matching method (IFM), developed by Matheney and Nowack (1995). This method was previously applied to ScS-S (Ford et al., 2012; Durand et al., 2013) and to PcS-S (Liu and Grand, 2018) differential measurements, aiming to find the differential anelastic delay $\delta t^*$ that equalizes the instantaneous frequencies of seismic phases by complex seismic trace analysis.

Measuring $\delta t^*$ between seismic waves recorded on a single seismogram is very efficient for canceling source effects and crustal effects near the receiver. However, thanks to the development of numerical methods for 3D wave propagation (Komatitsch and Tromp, 2002a,b), it is now possible to better account for the crust and focusing/defocusing effects due to the 3D elastic heterogeneities. In this study, we thus propose to compare the instantaneous frequency of observed and 3D synthetic seismograms. The synthetics are computed using SPECFEM (Komatitsch and Tromp, 2002a,b) in a 3D global model S40RTS (Ritsema et al., 2011) on top of which we added a global crustal model CRUST1.0 (Laske et al., 2013). Source parameters are taken from the Global Centroid-Moment-Tensor catalog (Ekstroem et al., 2012). The attenuation model of PREM, $Q_{\text{PREM}}$, is used for the synthetics (Dziewonski and Anderson, 1981).

We calculate the synthetics with a shortest period of 9 seconds. A large number of CPU hours were used, as a simulation takes $\approx 2$ hours per event (but each simulation provides synthetics for all the stations). Using our computing resources, the high-frequency synthetic calculations for all 357 events took $\approx 700$ hours ($\approx 29.7$ days), utilizing $\approx 1,713,600$ CPU hours with 2,400 processors running in parallel. We measure the $\delta t^*$ between observed and synthetic S waves filtered in the period range of 10-100 seconds.

The IFM method consists in applying the so-called "causal attenuation operator" $D(\omega)$ (Aki and Richards, 2002) to attenuate either the observed or the synthetic phase until their instantaneous frequencies become equal. The causal attenuation operator is

$$D(\omega) = \exp\left(-\frac{\omega \delta t^*}{2}(1 - \frac{2i}{\pi}\log\frac{\omega}{\omega_r})\right), \tag{1}$$

where

$$\delta t^* = \int_{path} \frac{1}{V_s}\left(\frac{1}{Q_\mu} - \frac{1}{Q_{\text{PREM}}}\right) \mathrm{d}s, \tag{2}$$

$\omega$ is frequency, $\omega_r$ a reference frequency, $V_s$ the S wave velocity. The operator takes into account both the decrease in amplitude and the phase shift due to attenuation. The equation (1) assumes that $Q_\mu$ and $\delta t^*$ are nearly constant in the band of frequencies that we consider (Cormier, 2020). The instantaneous phase and amplitude of the seismogram trace $y(t)$ (either observed or synthetics), $\phi(t)$ and $a(t)$, are obtained by computing its Hilbert transform $\hat{y} = H(y)$, so that the complex quantity $y(t) + i\hat{y}(t)$, expressed in polar form as $a(t)\exp[i\phi(t)]$, gives a representation of the original seismogram as an amplitude-modulated signal

$$y(t) = \text{Real}\left[a(t)\exp(i\phi(t)\right]. \tag{3}$$

The instantaneous frequency $f(t)$ of the amplitude-modulated signal is defined as the derivative of the phase

$$2\pi f(t) = \frac{\mathrm{d}\phi(t)}{\mathrm{d}t}. \tag{4}$$

Seismic phases are identified by looking for maxima of the envelop, $a(t)$, that are close to predicted arrival times. When a seismic phase is identified on both the observations and the synthetics, we search for the $\delta t^*$ of equation (1) that makes the instantaneous frequencies of their maxima equal, taking into account that the envelope maxima changes with $\delta t^*$. Notice that since $Q_\mu \geq 0$, $\delta t^*$ must be larger than $t^* = -\int_{path} 1/(V_s Q_{\text{PREM}})\,\mathrm{d}s$. Measurements that do not verify this inequality were removed. They generally correspond to short paths (mostly direct S) where attenuation is difficult to observe with good precision.

The advantage of the IFM method is that it does not require precise knowledge of the signal amplitude, which depends crucially on the magnitude and the focal mechanism of the earthquake source. An example is shown in Fig. 1. In the top panel (a), we show the observed (black), original 3D synthetic signal (red), and synthetic signal convolved with the causal operator (blue). Note the difference in amplitude and arrival time of the three signals. Their envelope time functions are shown in panel (b) and their instantaneous frequencies are shown in (c). The frequency of the observed signal (black) and that of the synthetic signal convolved with the causal operator (blue) are equal at their respective envelope maxima when $\delta t^* = 1.224$. For this $\delta t^*$, the observed signal and transformed signal corrected from its time delay and aligned at their envelope maxima are basically identical (black and blue curves, panel (d)). Although the raw synthetic signal and amplitude (red) was already close to the observation, it is clear that the application of the causal operator (blue) really improved the fit.

## 3. Synthetic tests

To validate the effectiveness of IFM, we carried out intensive tests for all seismic phases, with synthetic models. These tests were necessary for determining the most appropriate frequency band for the calculation of SPECFEM synthetics as well as the most appropriate epicentral distances for reliable measurements.

We thus calculate synthetics with various minimum periods in SPECFEM and test various bandwidths for the filtering of the observations and synthetics. We compare the results when two attenuation models are used, one with the attenuation structure of PREM, the other with another attenuation profile $Q_\mu$. The first one is used as a fake "synthetic", the second as a fake "observation". We applied the IFM and check to which precision we can recover the exact $\delta t^*$ between these two calculations. The velocity model in these tests was S40RTS. The quality of the measurements are, not surprisingly, improving when the precision of SPECFEM is increased by choosing a higher maximum frequency period. However as the computation time increases rapidly with the maximum frequency, we decided that 0.11 Hz (9 s) was the best compromise to achieve a high precision at a reasonable computational cost.

The synthetic tests have shown that $\delta t^*$ can be accurately recovered using several phases including S, ScS, $S_{diff}$, $S_n$, and $ScS_n$ and their depth phases with measurement errors smaller than $\pm 5\%$. We show in Fig. 2, an example of synthetic test where we reduced the attenuation of

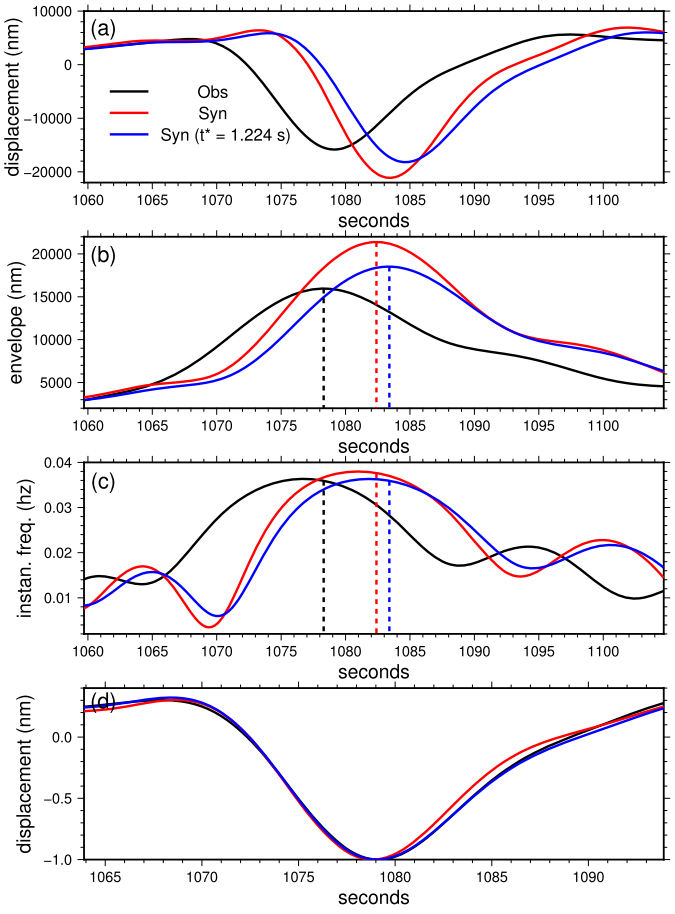


**Fig. 1.** Example of instantaneous frequency measurement. An observed S wave (black), recorded at the USArray station MNTX for a magnitude 6.8 Southern Bolivia earthquake that occurred in 2018 (epicentral distance: 66.1°), is compared with the corresponding synthetic (red) computed in a 3D model (S40RTS+CRUST1.0) (a). The blue curves correspond to the final synthetic convolved with the causal operator (eq. (1)). The amplitude and phase of the signals are shown in (b) and (c). For $\delta t^* = 1.224$ the phase of the synthetic convolved with the causal operator corresponds to the observed seismogram. The plot of the three signals, aligned with their amplitude maxima (d), shows the much better agreement between the observation and the synthetic with the chosen $\delta t^*$; black and blue curves are visually identical, while the synthetic computed with PREM (red), remains significantly different.

PREM by 20% in the fake observations. These seismograms are generated for a deep earthquake with focal depth of 600 km (left and middle columns). The right column is for a shallow earthquake with focal depth of 15 km. The Fig. 2 shows that $\delta t^*$ measurements are not reliable at certain epicentral distances and for some waves. For example, for shallow earthquakes, ScS in $1-35°$, $ScS_2$ in $1-85°$ and $ScS_3$ in $1-150°$, the $\delta t^*$ measurements are significantly far from predictions, because of the noise due to surface waves. We will exclude these data with those ranges of epicentral distance from the dataset. This is not the case for deep earthquakes where surface waves are not so strongly excited.

Fig. S1 illustrates the variations in $\delta t^*$ caused by mantle and crustal heterogeneities, acting separately. It shows the differences in $\delta t^*$ values measured between synthetic cases computed using 3D crust and mantle, and cases where either a 3D crust lies on a 1D mantle or a 1D crust is added on top of a 3D mantle. For this test, a synthetic deep earthquake is located at 370 km depth, at the equator and zero longitude. The $\delta t^*$ measured at stations spaced evenly in azimuthal directions, are averaged as a function of epicentral distance. The effects of the 3D mantle anomalies (blue circles) are moderate around 0.5 s; This is consistent with findings by Zhu et al. (2022) that the mean amplitudes of S waves and their multiples show small differences between 1D and 3D mantle models. However, the effects of the 3D crust (red circles) are much larger particularly for rays that cross the crust multiple times (for $sScS_3$ the difference amounts to around 4 s). This confirms that attenuation measurements must rely on accurate 3D models and that the effects of the crust are major. This explains why in Fig. 2, the multiple reflection phases, such as $S_3$ and $S_4$ (or $ScS_2$ and $ScS_3$), generally exhibit larger errors than single-bounce phases like S (or ScS) and why depth phases measurements (middle column, Fig. 2) have generally more uncertainty than direct phase measurements (left column, Fig. 2).

The apparent inferior quality of measurements for multiple reflection paths in numerical experiments with synthetics is, however, somewhat misleading. In the presence of noise or inaccurate focusing calculation, the effect of attenuation becomes more visible on longer paths (since $\delta t^*$ in (2) increases with distance). This favors the multiple reflections since, for a radial attenuation model, we should have

$$\delta t^*(S_n, n\Delta) \approx n\delta t^*(S, \Delta), \tag{5}$$

(the anelastic delay of a $S_n$ wave that has bounced $n$ times is $n$ times greater than that of a direct ray measured at the epicentral distance $\Delta$). This rule remains approximately true for all types of waves as we will see in the following, even when the measurements of the $\delta t^*$ in both sides of the previous equality, are measured for two earthquakes with different mechanisms and somewhat different epicenter depths (we simply classify the earthquakes as “deep” or “shallow” events).

## 4. Quality assessment

The selection of the data has been done starting from a total record of 357 earthquakes of magnitude 4.7-6.9 that occurred since 2009, including 154 deep earthquakes with focal depth > 100 km and 203 shallow earthquakes with focal depth < 33 km. Most of the earthquakes (304) have magnitudes between 5.5 and 6.9 to ensure a high signal–to–noise ratio and avoid too complex source-time functions. We include 53 smaller-amplitude (4.7-5.5) events for deep earthquakes in Eurasia and Atlantic Oceans aiming to expand the ray coverage (Fig. S2). We use either shallow (< 33 km) or deep (> 100 km) earthquakes. In the first case, S and sS are confused, as we show in Fig. 2, and this does not affect the $\delta t^*$ measurements. In the second case, S and sS are significantly separated and two reliable $\delta t^*$ measurements are made. We only work with the SH component seismograms to avoid the contamination of P and SV waves. We remove the instrument response and rotate the seismograms.

We identified the observed and synthetic S phases and measured their travel-time differences and excluded those exceeding 15 seconds, as these could be misidentifications. We restrict our analysis to S phases with signal-to-noise ratios (SNR) larger than 2, where the signal level was quantified as the average data amplitude in a 70-second window centered on the observed S phases, and the noise level was assessed from a 500-second window prior to the earthquake origin time. To avoid phase interferences, we discard all cases where several phases can arrive within a 30 s window. For phases with triplications, we only pick the first phase if it arrives at least > 50 seconds earlier than the following ones. We also measure the maximum envelope amplitude ratio between observed and synthetic phases and only keep those with ratios between 0.2 and 5. To further exclude potential noisy data, we measure the correlation between observed and SPECFEM synthetics and exclude those with correlation coefficients below 0.60. All these criterium of quality (frequency ranges, SNR, correlations, time delays) are based on the extensive synthetic tests that we performed.

## 5. Resulting global dataset

The different phases for which the $\delta t^*$ has been measured are plotted in Fig. S3 and are summarized in Table 1 and Fig. 3. In Fig. 3, for shallow events (panel (b)), the usual hodochron is recovered except for

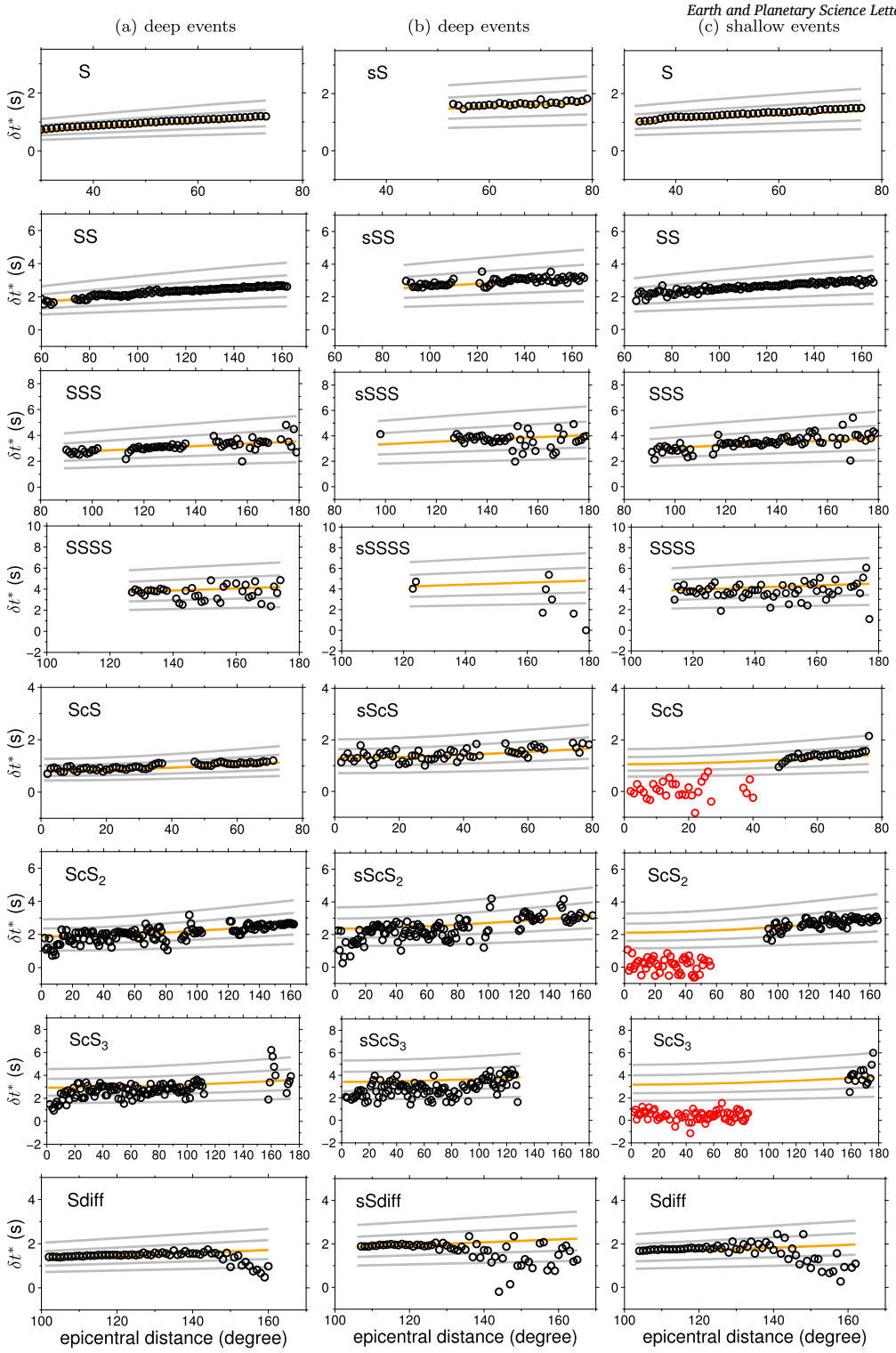


**Fig. 2.** Differential anelastic time delay for different waves, $\delta t^*$, measured with instantaneous frequency matching method at period range of $10-100$ s between a reference model (S40RTS, CRUST1.0 with $Q_{\mathrm{PREM}}$), and a revised model where $Q_\mu$ is reduced by 20% in the whole mantle. These synthetic tests consider a deep earthquake with focal depth of 600 km (left and middle columns) or a shallow earthquake with focal depth of 15 km (right column). The ray theory predictions are depicted with orange lines and gray lines represent errors of ±5% and ±10%. The absence of data points indicates phase interferences. Most of the measured $\delta t^*$ are within ±5% errors of the predictions except for ScS, $ScS_2$ and $ScS_3$ of shallow earthquakes in $1-40°$, $1-80°$ and $1-150°$ (red dots). The surface waves vigorously excited by shallow earthquakes forbid a correct measure of the $\delta t^*$ at short distances.

the epicentral distances where phase interference could occur. For deep events (panel (a)), the direct and reflected phase (e.g., ScS and sScS) are recorded. These measurements are all in an epicentral distance that minimizes possibility of phase interferences, their estimated signal-to-noise ratio are larger than 2 and the correlations between the observations and the SPECFEM synthetics are larger than 0.60. We potentially check ≈ half a million phase arrivals and only less than 10% of them (37,341) satisfied our selection criteria. They correspond to various possible phases that sample different depths in the mantle (see Table 1 and Figs. 3 or S3).

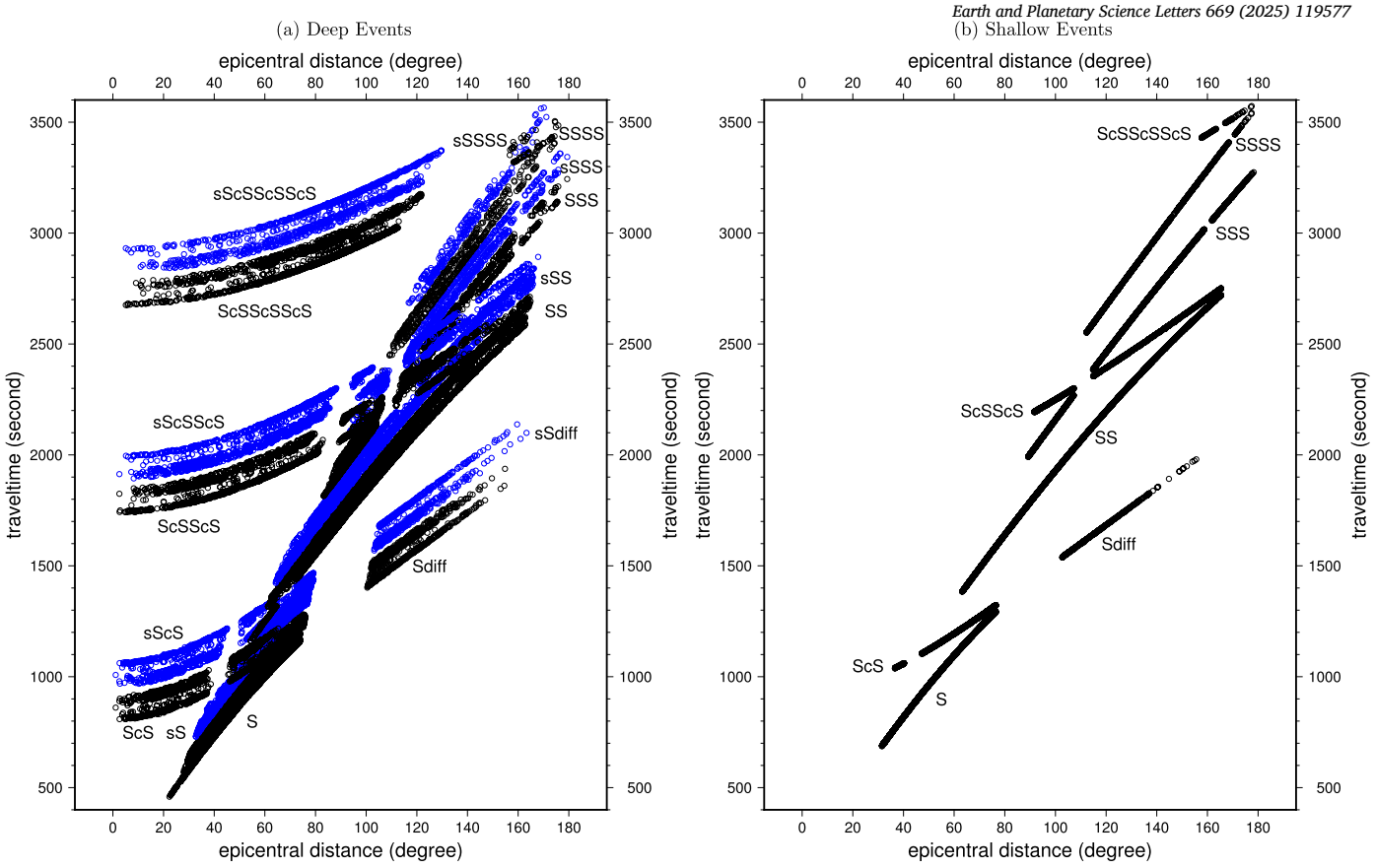


**Fig. 3.** Traveltimes with respect to epicentral distance for the selected data (correlation larger than 0.6, signal-to-noise ratio larger than 2, amplitude ratio between 0.2 and 5, time delays lower than 15 s). (a) for deep earthquakes (focal depth > 100 km) with black dots representing direct waves and blue dots as the depth phases; (b) for shallow earthquakes with focal depth < 33 km for which direct and depth phase are confused. The absence of data in some epicentral distance ranges indicates phase interferences or noisy data. For example, S and ScS waves in $80-100°$ for both deep and shallow earthquakes have close arrivals and phase interferences (a and b). For shallow events, ScS waves in $1-35°$, $ScS_2$ waves in $1-85°$ and $ScS_3$ waves in $1-150°$ interfere with surface waves (b).

**Table 1**
We consider more than 400,000 observations and only kept 37,341 of them according to our quality criteria.

| | All data | Selected data |
|---|---|---|
| S, sS | 33,276 | 7,805 |
| $S_2$, $sS_2$, $S_3$, $sS_3$, $S_4$, $sS_4$ | 154,275 | 17,394 |
| ScS, sScS | 34,806 | 3,225 |
| $ScS_2$, $sScS_2$, $ScS_3$, $sScS_3$ | 168,593 | 7,148 |
| $S_{diff}$, $sS_{diff}$ | 43,422 | 1,769 |
| Total | 434,372 | 37,341 |

The geographical density of the data is illustrated by the four panels of Fig. 4. In Fig. 4(a), we report the surface projection of the S and sS ray paths. The bottoming points of the $S_2$ and $sS_2$ are shown in panel (b), while those at the CMB, for the ScS, sScS and other phases reflected on the core are shown in panel (c). The samplings of the CMB by the $S_{diff}$ and $sS_{diff}$ are depicted in panel (d). The data set suffers from the usual geographical bias of global tomography with a higher ray density around the Pacific subductions and a lower density in the South hemisphere, but the coverage is reasonably sampling the whole mantle.

Despite the care taken in selecting the data, the dispersion of the measurements is large (see Fig. S3), comparable to what was obtained in previous attempts, underlining once again the difficulty of measuring attenuation. Some of this dispersion may however be due to the presence of 3D attenuation anomalies, which we do not consider in this article.

Since our aim is to build a 1D model of attenuation, we expect that for each type of wave, the $\delta t^*$ should only be a function of the epicentral distance. We therefore average the $\delta t^*$ for all measurements of a given phase, corresponding to similar epicentral distances, using a moving averaging window of $\pm 5°$. The variance of the data, $\sigma$, and that of the mean, $\overline{\sigma} = \sigma/\sqrt{n-1}$, are calculated ($n$ is the number of observations in each bin of the moving window).

## 6. First considerations before a 1D inversion

In Fig. 5 we show the resulting mean $\delta t^*$ as a function of the epicentral distance for various types of waves. The epicentral intervals where no measurements are made correspond to situations where there are no phases, where wave triplications or interferences occur or generally where the synthetic tests have shown that the measurements are unreliable (Fig. 2).

One obvious observation from Fig. 5 is that the observed mean $\delta t^*$ are most often negative, indicating that the mantle is less attenuating than PREM (PREM predictions correspond to the thin dashed line at $\delta t^* = 0$). By multiplying $Q_{\mathrm{PREM}}$ by 1.2, we can adjust the averages of the observations (black dashed line) but this does not adjust the trends.

One feature that $Q_{\mathrm{PREM}}$, $1.2\times Q_{\mathrm{PREM}}$, or all 4-layers models with stratification similar to that of PREM cannot explain (to wit, lithosphere, asthenosphere, transition zone and lower mantle), is the presence of a bump in the $\delta t^*$ for all S, $S_n$, sS, $sS_n$ phases, at a specific epicentral distance. To make this feature more conspicuous, we plot observations together, for all $S_n$ of deep earthquakes, all $sS_n$, and all $S_n$ of shallow earthquakes, using equation (5). For example, we take the values for $S_n$ from Fig. 5, divide the $\delta t^*$ and epicentral distance $\Delta$ by $n$, average the $\delta t^*$ in $\pm 5°$ intervals and plot them. All these waves are bottoming up in the mantle and the depth of the turning point is a simple function of the

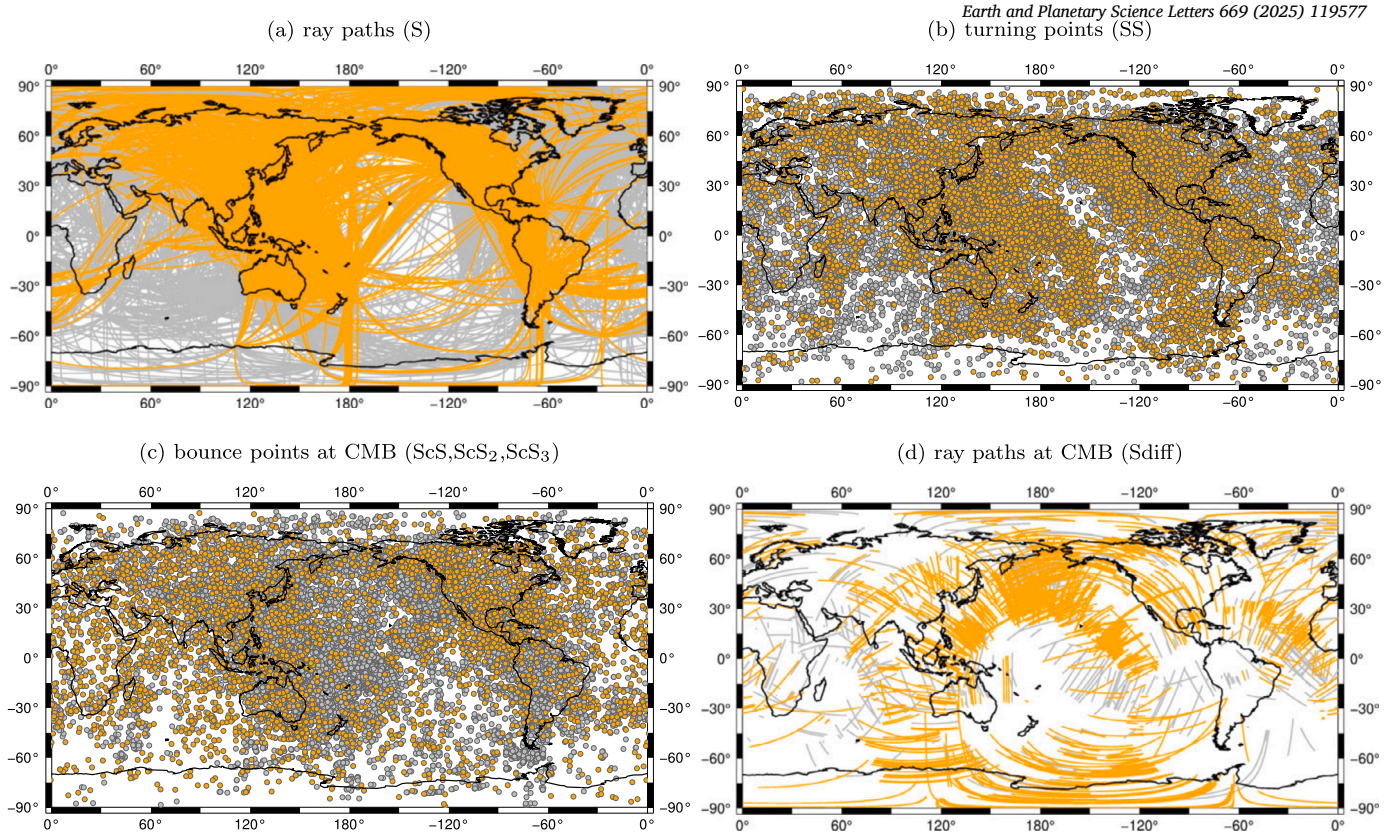


**Fig. 4.** The different panels show the projections of the S and sS paths on the surface (a), the bottoming points of the $S_2$ and $sS_2$ (b), the bounce points on the $ScS_n$ and $sSsS_n$ on the CMB (c), the projection of the $S_{diff}$ and $sS_{diff}$ paths on the CMB (d). The gray rays or dots represent data for shallow earthquakes, the orange for deep earthquakes. All the data plotted are high quality data with correlation larger than 0.60, signal to noise ratio larger than 2, amplitude ratio between 0.2 and 5, and time delays lower than 15 s. The dataset in this study has a global coverage both in upper and lower mantle.

epicentral distance. All these data are plotted on Fig. 6 as a function of normalized epicentral distance (bottom axis) or bottoming depth (top axis). Clearly, all these data exhibit a hump corresponding to an attenuating layer located between 900 and 1200 km depth. A maximum of $\delta t^*$ must correspond to a minimum of quality factor.

In Fig. 6, depth phases (sS, $sS_2$,...) are systematically associated with a less negative $\delta t^*$ than direct phases. This is more evident for phases where the s-leg represents a greater proportion of the total path (sS, $sS_2$) than for $sS_3$ or $sS_4$ where the attenuation along the s-leg is a minor contributor to total attenuation. We believe that this feature indicates a larger attenuation (lower $Q_\mu$) in the slab corner, which will require the construction of a 3D attenuation model.

The $S_{diff}$ observations deserve a few comments. The $S_{diff}$ are natural extensions of S and ScS phases when these rays hit the CMB (see the hodochrons of Fig. 3). The $\delta t^*$ values at the shortest distance for $S_{diff}$, should therefore coincide with the $\delta t^*$ values for S or ScS at their greatest epicentral distance. This is more or less the case, with common values around -1.5 s. At longer distance, the attenuation of the $S_{diff}$ propagating along the CMB, should be related to the attenuation at the CMB and to the length of the path along the CMB with a slope (in s rad$^{-1}$)

$$\frac{\mathrm{d}\delta t^*}{\mathrm{d}\Delta} = \frac{R_{\mathrm{CMB}}}{V_s^{\mathrm{CMB}}}\left(\frac{1}{Q_\mu^{\mathrm{CMB}}} - \frac{1}{Q_{\mathrm{PREM}}}\right), \tag{6}$$

according to equation (2). The slopes measured from Fig. 5, unfortunately lead to negative values of $Q_\mu^{\mathrm{CMB}}$ for the deep events and to an extremely large $Q_\mu^{\mathrm{CMB}}$ for the shallow events; in fact, we find no evidence for attenuation along the CMB by comparing the seismogram with PREM predictions. We suggest that this is because the amplitude of the diffracted waves are strongly dependent of the details of the S wave velocity in D". Depending on the sign of the velocity gradient in D" and the presence of a discontinuity on top of D", both very uncertain (see e.g., Lay, 2007), seismic waves can be trapped along the CMB, totally altering their amplitude (Doornbos and Mondt, 1979). We therefore remove the $S_{diff}$ waves from the inversion although the $\delta t^*$ resulting from our model are reported in Fig. 5 with predicted slopes $\mathrm{d}\delta t^*/\mathrm{d}\Delta$ necessarily lower than those observed.

## 7. The inversion procedure

The $\delta t^*$ that we measured is related to the attenuation through the equation

$$\delta t^* = g(Q_\mu) = \int_{path} \frac{1}{V_s}\left(\frac{1}{Q_\mu} - \frac{1}{Q_{\mathrm{PREM}}}\right)\mathrm{d}s, \tag{7}$$

where $Q_\mu$, the attenuation structure, is unknown. Note that while the measurements are not dependent on ray theory, being computed with SPECFEM, ray theory is employed in the inversion. The integral is performed along the ray path, and $s$ is the abscissae along the ray. The velocity $V_s$ is either taken from a 1D model or from a 3D model (Ritsema et al., 2011). Practically the same results are obtained in both cases since the variations in $Q_\mu$ are much larger than those of $V_s$. Instead of inverting for $Q_\mu$, we prefer to look for $\log Q_\mu$, a parameterization that allows larger variations for the attenuation and guaranties to avoid negative values in the inverted $Q_\mu$ model. We discretize $\log Q_\mu$ using $k_{max}$ nodes at radii $R_k$, so that $\log Q_\mu(R_k) = p_k$, ($R_1$ and $R_{kmax}$ are the core-mantle boundary radius and the Earth's radius). A continuous expression for $Q_\mu$ is obtained with

$$\log Q_\mu = \sum_k p_k f_k(r), \tag{8}$$

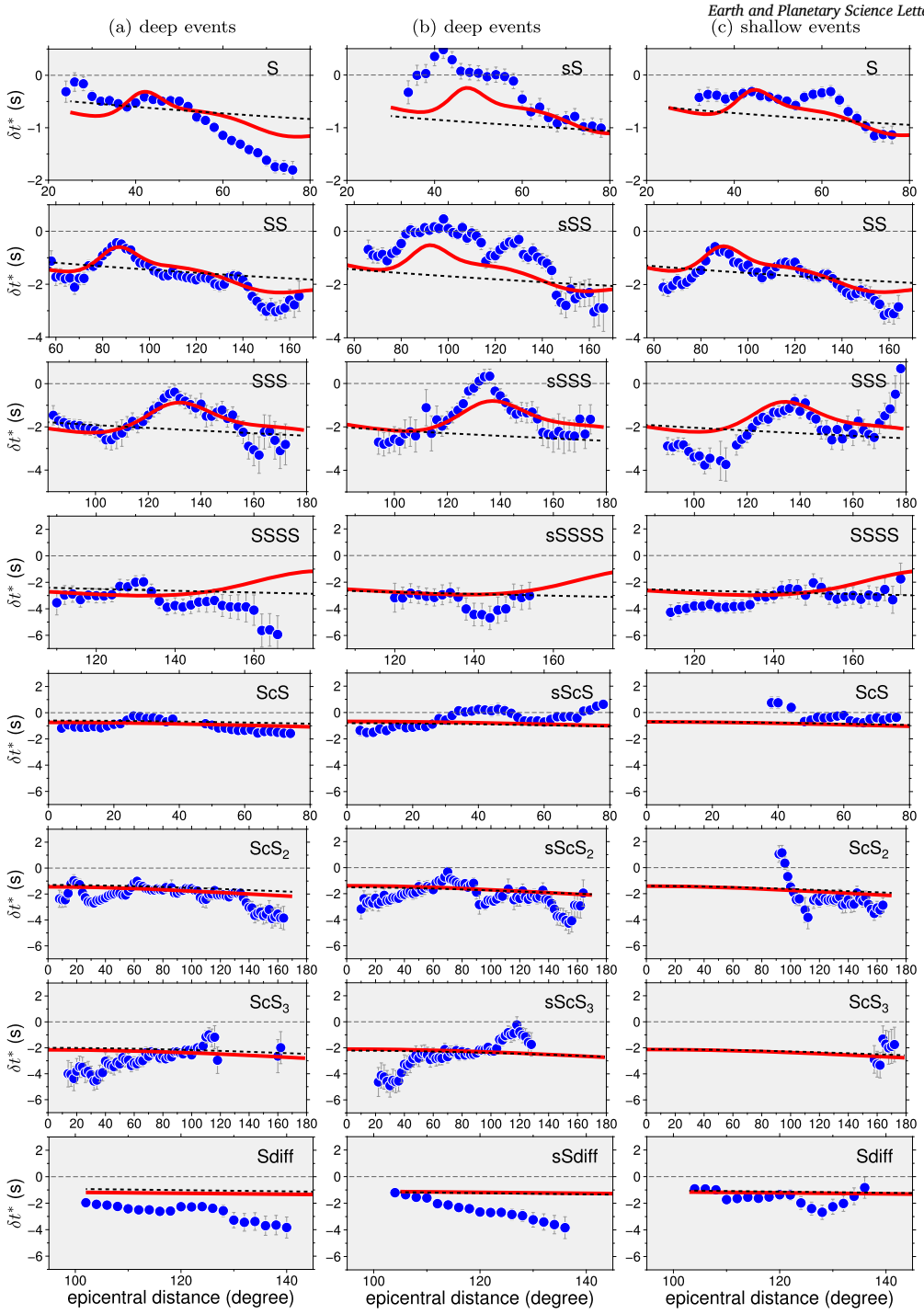


**Fig. 5.** Observed mean $\delta t^*$ (blue circle) as a function of the epicentral distance for different types of waves. Error bars show the $\overline{\sigma}$ estimates. Negative $\delta t^*$ can be observed for most waves, indicating less attenuation than in PREM (thin dashed line). The black dashed line is for a simple three-layer model with $Q_\mu = 1.2 \times Q_{\mathrm{PREM}}$ under the lithosphere. The absence of data in certain epicentral distance ranges indicates phase interference or noisy data. Predictions from our final model $Q_{L1D}$ (Fig. 8) are depicted by the red lines. The poor fit for $S_{diff}$ waves is due to the fact that these data are not inverted (see section 6).

where the radial functions $f_k(r)$ are cubic spline functions of the radius $r$. The functions $f_k(r)$ and their two first derivatives are continuous, defined between nodes by cubic polynomials, and such that $f_k(R_{k'}) = \delta_{kk'}$ ($\delta_{kk'} = 0$ is the Kronecker symbol). The parameters to invert are the $p_k$. These coefficients will be solved iteratively, and we will obtain a converging series of estimates $Q_\mu^i$, where $i$ is the number of iterations, depending on the $p_k^i$ (also noted as $\mathbf{p}^i$, $\mathbf{p}^0$ is therefore the starting model). One has therefore for the ray $j$, following the path $j$,

$$g_j(Q_\mu) = g_j(\mathbf{p}^i) = \int_{path_j} \frac{1}{V_s} \left( \exp\left( -\sum_k p_k^i f_k(r) \right) - \frac{1}{Q_{\mathrm{PREM}}} \right) \mathrm{d}s. \tag{9}$$

At iteration $i$, the partial derivatives of $g$ with respect to the parameter $p_k^i$, are

$$G^i = -\int_{path_j} \frac{f_k(r)}{V_s Q_\mu} \mathrm{d}s. \tag{10}$$

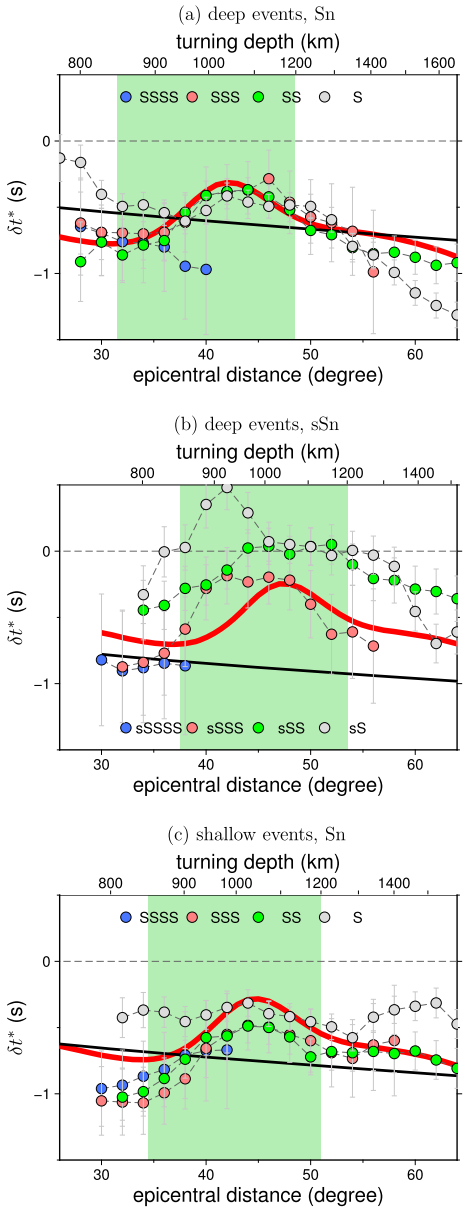


**Fig. 6.** Observed and normalized $\delta t^*$ as a function of epicentral distances and turning depths for multiple S and sS waves. For each wave type, the bottoming depth or the ray in the mantle is a simple function of the epicentral distance. Using (5), the anelastic delays for phases with $n$ surface reflections and epicentral distance $\Delta$ were divided by $n$, averaged over $\pm 5°$ intervals, and plotted at $\Delta/n$. This highlights a common hump of the observations in the turning depth range 850-1200 km (green shaded zone). The predictions for PREM and for a model where the quality factor of PREM has been multiplied by 1.2, are indicated in thin dashed and solid black lines, and for our final model, in red.

Following Tarantola and Valette (1982),

$$\mathbf{p}^{i+1} = \mathbf{p}^0 + (G^{t,i} \cdot C_{dd}^{-1} \cdot G^i + C_{pp}^{-1})^{-1} \cdot G^{t,i} \cdot C_{dd}^{-1} (\delta \mathbf{t}^* - g(\mathbf{p}^i) + G^i(\mathbf{p}^i - \mathbf{p}^0)), \tag{11}$$

where $G^{t,i}$ is the transposed of $G^i$. $C_{dd}$ and $C_{pp}$ are the a priori data and model covariance matrices, respectively.

Note that although $Q_{\text{PREM}}$ disappears in the term $\delta \mathbf{t}^* - g(\mathbf{p}^i)$, the final model remains constrained to be close to $Q_{\text{PREM}}$ when we use PREM as the priori model $\mathbf{p^0}$. We indeed assume that the final model of attenuation cannot not be in large contradiction with PREM, based on normal modes and surface wave observations. The thin, low attenuation lithosphere present in PREM is in fact invisible to body waves whose paths are close to normal near the surface. Its presence in our model is mainly due to the fact that it is already included in the a priori model.

Convergence is generally achieved after 5 to 10 iterations. The choices of the starting model, $\mathbf{p}^0$, the data and parameter covariances are discussed in the next section. The quality of the inversion is quantified either by the final parameter covariance matrix $\widehat{C}_{pp}$

$$\widehat{C}_{pp} = (G^{t,i} \cdot C_{dd}^{-1} \cdot G^i + C_{pp}^{-1})^{-1}, \tag{12}$$

or by the resolution matrix $R$

$$R = Id - \widehat{C}_{pp} C_{pp}^{-1}, \tag{13}$$

(a perfect resolution corresponds to $R = Id$, the identity matrix, the non diagonal terms of $R$ indicate trade-offs between the inverted parameters). We define the obtained radial profile of $Q_\mu$ as $Q_{L1D}$ and its uncertainty is of order

$$\frac{\Delta Q_{L1D}}{Q_{L1D}} = \left( \mathbf{f}(r) \cdot \widehat{C}_{pp} \cdot \mathbf{f}(r) \right)^{1/2}, \tag{14}$$

where $\mathbf{f}(r)$ is the vector containing the values of the $k$ splines as a function of $r$ (the expression is only valid at first order, as if the inversion were linear).

## 8. 1D attenuation

We use the mean data $\delta t^*$ from Fig. 5 with their uncertainties $\overline{\sigma}$, to build a 1D attenuation model. As previously discussed, the core diffracted observations are excluded. The data covariance matrix is diagonal with elements $\overline{\sigma}^2$ and the model covariance matrix is also diagonal with elements $\sigma_p^2$ (we also performed inversions where this covariance matrix accounted for the partial overlap of the spline functions and their varying widths with no notable differences). In this inversion, the a priori model is a smooth depth-dependent model approximating PREM. We could have used directly PREM but as the inversion is in term of splines, we consider more appropriate to project PREM onto our spline basis and use this smooth approximation as a starting model. We use 20 nodes to define the splines and the separation of the nodes increases linearly with depth, from 77 to 220 km. The depths of the nodes are listed in Supplementary Table S1. The spline functions are shown in Fig. S4. They gently oscillate around zero except near $R_k$. The smooth approximation of PREM is constructed by summing the spline basis functions, each weighted by the corresponding PREM $Q_\mu$ values (see equation (8)).

For the velocity model $V_s$ we used either PREM or the 3D S40RTS model without noticing any visible difference in the results since the $Q_\mu$ variations are much larger than the $V_s$ heterogeneities. We also accounted for the dependence of $V_s$ with $Q_\mu$, the physical dispersion (see Kanamori and Anderson, 1977), which is also a negligible effect. Finally, the effect of upper mantle anisotropy is likely to be negligible. We are only using SH waves and the few percent changes in velocity that can be expected over 200-300 km thick layers at the top and bottom of the mantle remain small compared with variations in $Q_\mu$, and their effect in (2) can be neglected. This is confirmed by previous studies reporting that anisotropy corrections lead to $\delta t^*$ corrections of the order of 0.3 s (Ford et al., 2012; Durand et al., 2013). The splitting of the waves by anisotropy which broadens the SH component, should also increase the apparent attenuation (Cormier, 2020). However, our observations indicate otherwise: a lower attenuation than in PREM. This further suggests that the effect of anisotropy is minimal.

To select the model uncertainties, $\sigma_p$, (i.e., the uncertainties of $\log Q_\mu$ on the spline nodes, corresponding to the distance permitted, away from PREM), we performed various tests. The goodness of fit of the data is measured by $\chi$,

$$\chi^2 = \frac{1}{n} \sum_{i=1}^{n} \frac{(t_i^* - t_{i,pred}^*)^2}{\overline{\sigma}_i^2}. \tag{15}$$

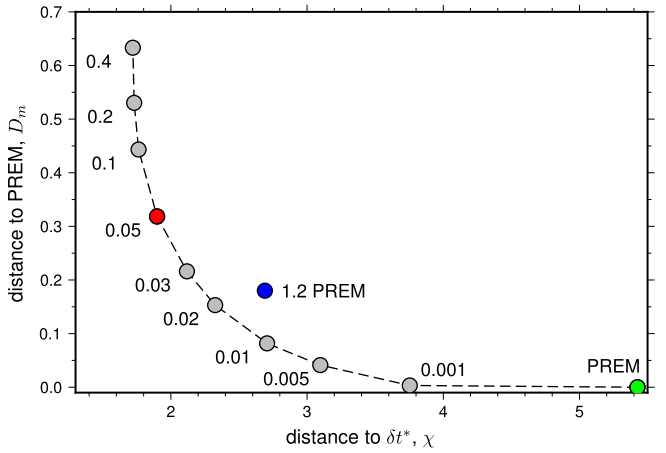


**Fig. 7.** Trade-off between fitting the data, $\chi$, and remaining close to PREM, $D_m$. These two quantities are plotted parameterized by the value of $\sigma_p$ indicated along the grey dots. PREM predictions (green dot, with $D_m = 0$) are far away from our observations. Multiplying the quality factor of PREM by 1.2, decreases $\chi$. We choose $\sigma_p = 0.05$ in the following (the other cases are discussed in the Supplementary Fig. S5).

It quantifies the average distance between observations and predictions, measured in terms of the error bar $\overline{\sigma}_i$. An increase in $\sigma_p$ allows a better fit but increases the distance from PREM measured by

$$D_m^2 = \frac{1}{k_{max}} \sum_k (p_k - p_k^0)^2 \tag{16}$$

These tests are summarized by the L-curve of Fig. 7. In this figure, we show the $\delta t^*$ misfits when the attenuation of PREM is used (green dot), when the quality factor of PREM is multiplied by 1.2 (blue dot, with $D_m = \log 1.2$), and the results of our inversion depending on the value of $\sigma_p$ (grey dots). We choose $\sigma_p = 0.05$ in the following, that seems a reasonable compromise (see models with different $\sigma_p$ in Supplementary Fig. S5). PREM predictions are clearly far from our body wave observations. By simply multiplying $Q_{\text{PREM}}$ by 1.2 a much better fit is obtained, however our model further decreases $\chi$ by a significant proportion (30%). The final $\chi$ remains larger than 1, however, which means that the predictions are not within the error bars of the observations; we believe this is largely due to lateral variations in attenuation indicated by the large difference between depth phases (sS, sScS...) and direct phases (S, ScS...) (see Fig. 5).

The chosen model, $Q_{L1D}$, is depicted in Fig. 8 (red curve with shaded uncertainties). The corresponding spline coefficients are listed in Supplementary Table S1. The predicted $\delta t^*$ values were shown in Fig. 5 and we report in Table S2 the $\chi$ obtained for each type of waves, and for all the data set (we included the CMB diffracted waves in calculating the total $\chi$). The most notable characteristics of our model is the presence of an attenuating layer at 1000 km depth that imposes the hump of the observed $\delta t^*$ previously discussed. This attenuating layer is not related to the choice of the reference value and is present even when instead of using PREM as a reference model we use other reference models (see supplementary Fig. S6). A low-attenuation (high $Q_\mu$) zone at $\sim$ 1900 km is also observed in model $Q_{L1D}$. This feature is consistent with the observed increase in the slope of $\delta t^*$, towards more negative values, for all types of $S_2$ waves and S waves around 140° and around 70°, respectively, as shown in Fig. 5, which roughly corresponds to a turning depth of $\sim$ 1900 km. We notice that $1.2 \times Q_{\text{PREM}}$ and $Q_{L1D}$ models improve the data fit of $S_{diff}$ (Table S2) even though they are not included in the inversion. Adding the $S_{diff}$ data to the inversion leads to a very similar profile except for a sharp increase of the $Q_\mu$ value at the CMB (we have seen that the dataset does not record any noticeable attenuation there and hence, suggests $Q_\mu^{\text{CMB}} = \infty$).

The shading around $Q_{L1D}$, in Fig. 8, indicates the uncertainties according to (14). They are minimal around 1000 km depth where the model is well resolved. This is confirmed by the resolution matrix (see Fig. S7). The resolution matrix does not indicate significant trade-offs between layers. The resolution is very good from 600 to 2000 km depth, reasonable in the asthenosphere and the deep mantle, and poor from 300 to 600 km depth and in the lithosphere where our model is primarily constrained by the a priori PREM model.

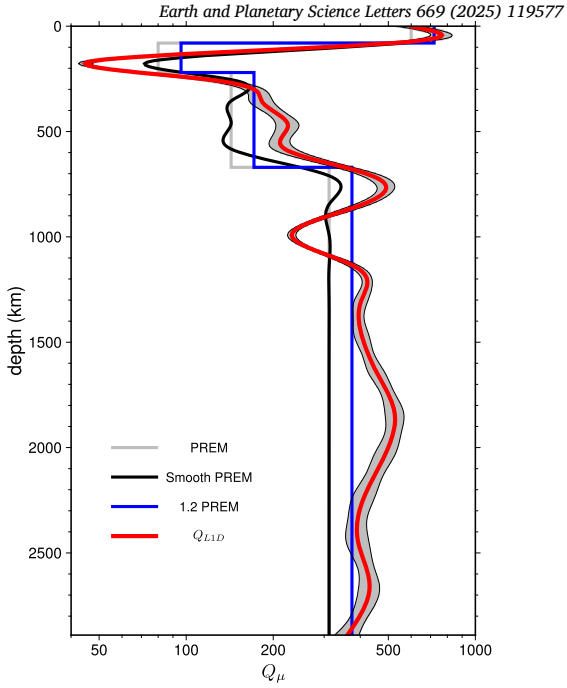


**Fig. 8.** $Q_{L1D}$ model inverted (red), gray shading indicates the model uncertainty according to eq. (14). PREM model is plotted in grey for reference and in blue when multiplied by 1.2. The smooth model approximating PREM using spline functions is plotted in black. The strong oscillation of $Q_\mu$ on top of the lower mantle at $\sim$ 1000 km is a very stable feature for which the uncertainties are minimal. A low attenuation (high $Q_\mu$) at approximately 1900 km is also suggested.

## 9. Discussion and conclusion

Seismic attenuation remains a difficult quantity to measure, and attenuation tomography is only in its infancy, with resolution comparable to that of $V_s$ tomography was in the 1980s (Dziewonski, 1984). The amplitude of a seismic phase depends on the seismic moment of the earthquake, the propagation distance and the focalisation/defocalisation of the wavefront deformed by the velocity anomalies. Using SPECFEM, a tomographic model like S40RTS, and the 3D CRUST1.0 model should take into account the focalisation due to large-scale heterogeneities. Seismic scatterers, which are not mapped by current tomographic models, also affect wave amplitude but this extrinsic attenuation is probably a minor ($\leq$ 10%) component (see, Ricard et al., 2014). deSilva and Cormier (2020) suggest that scattering could contribute up to 43% of the total attenuation for $ScS_n$ waves with a dominant frequency of 0.05 Hz, which is a somewhat larger effect. However, part of their estimate is due to effects that should be accounted for by our 3D SPECFEM synthetics. Working with phases rather than amplitudes should also reduce the dependence of the signal to the uncertainties of the seismic moment. We therefore believe that our large database of $\delta t^*$ values provides a more homogeneous and higher quality dataset of body-wave than previously obtained.

Fig. 9 compares our $Q_\mu$ model with several other radial models of quality factors obtained from body wave measurements (panel a), and long period measurements (panel b). The differences between all these models are large, but we can nevertheless draw some conclusions.

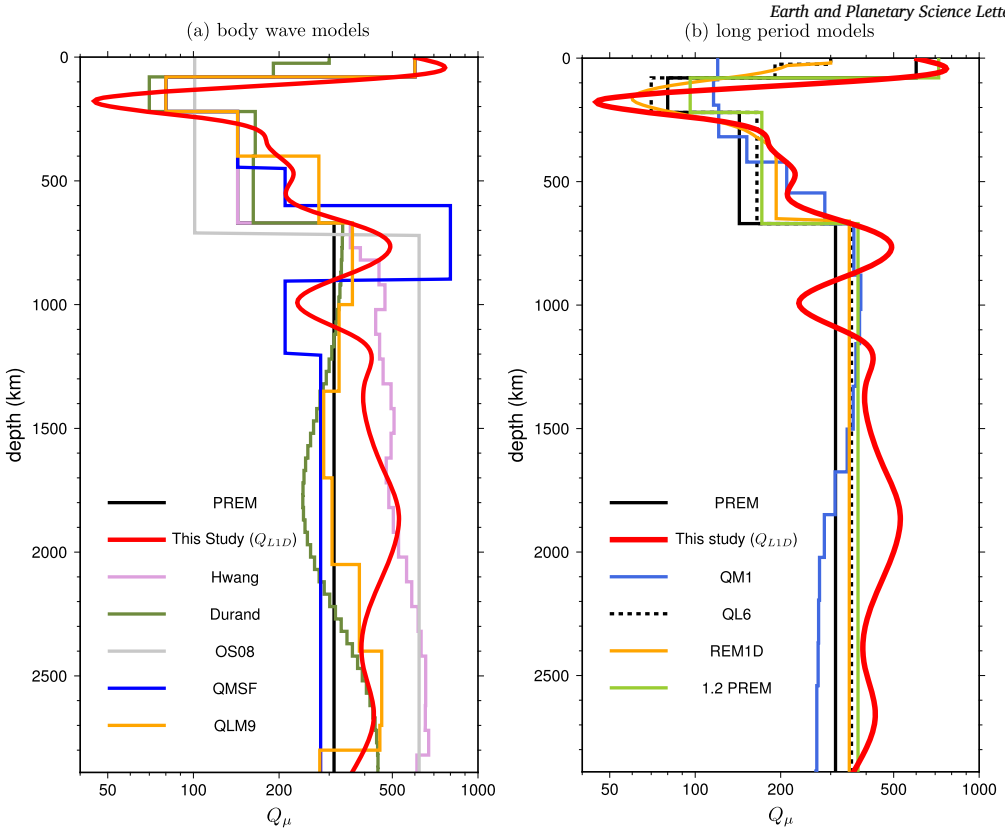


**Fig. 9.** Panel (a) various radial models of the quality factor $Q_\mu$ in the mantle obtained from body wave measurements (QLM9 (Lawrence and Wysession, 2006), Hwang (Hwang and Ritsema, 2011), Durand (Durand et al., 2017), OS08 (Oki and Shearer, 2008), QMSF (Zhu et al., 2022)). PREM model (Dziewonski and Anderson, 1981) is also plotted for reference. Panel (b) models from long-period wave measurements including PREM, QM1 (Widmer et al., 1991), QL6 (Durek and Ekstrom, 1996) and REM1D (Moulik and Ekstrom, 2025).

• All models agree on a narrow and shallow zone of attenuation under the plates, between 100 and 200 km deep, where $Q_\mu$ might be as low as 50. While teleseismic body waves have limited resolution in the lithosphere, the very low $Q_\mu$ values in the asthenosphere (as in PREM) significantly alter the average $\delta t^*$ measurements, making the inversion sensitive to changes in this zone (see the resolution matrix of Fig. S7). To investigate this further, we removed the low-Q zone between 80 – 220 km from the a priori model; the resulting inverted model still recovered a low-Q feature within this depth range (see Fig. S6). High attenuation in the asthenosphere may reflect elevated temperatures and potential partial melt. This reduces viscosity and enable the asthenosphere to act as a decoupling layer beneath the lithosphere (Debayle et al., 2020; Sun and Zhou, 2023).

• From this low $Q_\mu$ layer down to 670 km depth, the quality factor around 200 is larger than PREM ($Q_{\text{PREM}} = 143$) (in agreement with the findings of Widmer et al., 1991; Lawrence and Wysession, 2006; Moulik and Ekstrom, 2025). It does not seem uniform but increases with depth. However, the resolution is limited in the 220 – 670 km depth range (see Fig. S7), where the inverted $Q_\mu$ structure is highly sensitive to the choice of a priori model. As shown in Fig. S6, the a priori models I, II and III — with constant $Q_\mu$ values of 200 and 400, or with a linear increase between 220 – 670 km, — produce significantly different inverted structures within this depth interval.

• Most models suggest a higher quality factor in the lower mantle than PREM ($Q_{\text{PREM}} = 312$). This is particularly evident in models based on body-waves, which report values of up to ~ 700 (e.g., Oki and Shearer, 2008; Lawrence and Wysession, 2006; Hwang and Ritsema, 2011), but also, to a lesser extent, for various long-period models (see Fig. 9) which suggest values around 350 (e.g., Durek and Ekstrom, 1996; Moulik and Ekstrom, 2025). The 3D model based on normal modes by Talavera-Soza et al. (2025) also predicts an average $Q_\mu$ higher than PREM in the lower mantle.

Assuming $Q_\mu^{-1} \propto \omega^{-\alpha}$ (Lekić et al., 2009), larger quality factors are expected for body waves than for modes and long-period waves. Lekić et al. (2009) suggest that $\alpha$ should be 0.3 at around 10 s, and decrease to 0.1 for periods of a few 100 s. Our dataset is based on seismograms filtered within a period range of 10 – 100 s and the dominant periods of the measurements are likely close to the shortest periods included, say around 10 – 30 s. In the lower mantle, we obtain $Q_\mu \approx 450$. Considering that the dominant period is around 300 s for the modes used in PREM ($Q_{\text{PREM}} = 312$), we infer a value of $\alpha \approx 0.11 - 0.16$. If instead we compare our model to the long period models such as QL6 or REM1D ($Q_\mu \approx 350$), we obtain a value $\alpha \approx 0.07 - 0.11$. Therefore, our seismic observations suggest a low value of $\alpha$ and a weak dependence of attenuation on frequency.

Our model is characterized by a high attenuation (low $Q_\mu$) around 1000 km which was revealed by the observations even before proper inversion. This feature was also present in Zhu et al. (2022) (Fig. 9), although they focused instead on the low-attenuation zone at 600—900 km using $S_n$ amplitudes and did not include 3D crustal model, $ScS_n$ phases or used the more sophisticated IFM method we implemented. Choy and Cormier (1986) had also indicated that the mid-mantle (400 – 1600 km depth) contributes primarily to the attenuation of low frequency waves in the 0.01 – 0.1 Hz range.

To confirm that our 1D inversion, which is based on ray theory, is unaffected by finite frequency effects and to assess the resolvability and robustness of a high-attenuation layer near the top of the lower mantle, we performed forward simulations using SPECFEM. We considered a simple quality factor model that was 1.2 $\times Q_{\text{PREM}}$, except in a low-$Q_\mu$ zone ($Q_\mu = 250$) at depths between 800 and 1200 km. This simple model mimics $Q_{L1D}$ (see Fig. S8). The resulting differential $\delta t^*$ mea-

surements, relative to PREM, exhibit a clear and consistent bump for all S waves and their multiples, in agreement with ray theory predictions (compare Figs. 5 and S8).

A real discontinuity at ∼ 1000 km is not present in seismic velocity or density models of the mantle at this depth but some changes around this depth has been noticed in the heterogeneity spectra of tomographic models, e.g., in SEISGLOB2 (Durand et al., 2017) or in SEMUCB-WM1 (French and Romanowicz, 2014) and some negative cross-correlation below and above this depth has been observed in S362WMANI+M (Moulik and Ekstroem, 2014). Several studies have also reported the widespread presence of scatterers at depths of 800-1300 km (Waszek et al., 2018; Jenkins et al., 2017; Zhang et al., 2023). This depth does not appear to correspond to an expected major mineralogical transformation although the garnet phase can persist deeper than the 670 km depth, before its complete transformation in perovskite (although this transformation should be finished before 800 km (Stixrude and Lithgow-Bertelloni, 2005)). The Clapeyron slope of the mineralogical transformation around 670 km is also known to hinder convective motion. This may force upwelling hotspots to pond beneath the upper-lower mantle interface and therefore form a hot layer of greater temperature (Schubert et al., 1995), more pyroxenic composition (Weinstein, 1992; Mambole and Fleitout, 2002), and perhaps more attenuation. The detection of a high-attenuation (low $Q_\mu$) zone at approximately 1000 km depth aligns with the global observation of a low-viscosity layer at a similar depth (Kido and Čadek, 1997; Rudolph et al., 2015). The top of the lower mantle may therefore have an attenuation profile reminiscent of that of the lithosphere-asthenosphere, with an attenuating layer underneath a more elastic shell.

## CRediT authorship contribution statement

**Shuyang Sun:** Writing – review & editing, Visualization, Validation, Investigation, Formal analysis, Data curation, Conceptualization. **Yanick Ricard:** Writing – review & editing, Writing – original draft, Visualization, Validation, Supervision, Methodology, Investigation, Formal analysis, Data curation, Conceptualization. **Stéphanie Durand:** Writing – review & editing, Validation, Supervision, Methodology, Investigation, Formal analysis, Data curation, Conceptualization. **Eric Debayle:** Writing – review & editing, Validation, Supervision, Resources, Project administration, Investigation, Funding acquisition, Formal analysis, Conceptualization.

## Declaration of competing interest

The authors declare that they have no known competing financial interests or personal relationships that could have appeared to influence the work reported in this paper.

## Acknowledgements

This work has been supported by the French ANR JIGSAW2 ANR-20-CE49-0001-01. We thank the reviewers, Göran Ekström and Vernon Cormier, for their thorough and constructive reviews.

## Appendix A. Supplementary material

Supplementary material related to this article can be found online at https://doi.org/10.1016/j.epsl.2025.119577.

## Data availability

Raw seismic waveforms used in this study are available from the IRIS platform (https://ds.iris.edu/ds/nodes/dmc/). Data preparation and preprocessing used the Seismic Analysis Code (https://ds.iris.edu/ds/nodes/dmc/software/downloads/sac/). Figures were made with the Generic Mapping Tools (GMT) package (Wessel and Smith, 1995). The model $Q_{L1D}$ can be accessed from https://zenodo.org/records/15869054.

## References

Aki, K., Richards, P.G., 2002. Quantitative Seismology, 2nd edition. University Science Books.
Bhattacharyya, J., Masters, G., Shearer, P., 1996. Global lateral variations of shear wave attenuation in the upper mantle. J. Geophys. Res., Solid Earth 101 (B10), 22273–22289.
Chan, W.W., Der, Z.A., 1988. Attenuation of multiple scs in various parts of the world. Geophys. J. Int. 92 (2), 303–314.
Chaves, C.A.M., Ritsema, J., 2016. The influence of shear-velocity heterogeneity on scs2/scs amplitude ratios and estimates of q in the mantle. Geophys. Res. Lett. 43 (15), 7997–8005.
Choy, G.L., Cormier, V.F., 1986. Direct measurement of the mantle attenuation operator from broadband p and s waveforms. J. Geophys. Res., Solid Earth 91 (B7), 7326–7342.
Cormier, V.F., 2020. Seismic viscoelastic attenuation. In: Encyclopedia of Solid Earth Geophysics. Springer, pp. 1–14.
Debayle, E., Bodin, T., Durand, S., Ricard, Y., 2020. Seismic evidence for partial melt below tectonic plates. Nature 586, 555–559.
deSilva, S., Cormier, V.F., 2020. The relative contributions of scattering and viscoelasticity to the attenuation of s waves in Earth's mantle. Solid Earth 11 (1), 161–171.
Doornbos, D.J., Mondt, J.C., 1979. P and s waves diffracted around the core and the velocity structure at the base of the mantle. Geophys. J. Int. 57 (2), 381–395.
Durand, S., Debayle, E., Ricard, Y., Zaroli, C., Lambotte, S., 2017. Confirmation of a change in the global shear velocity pattern at around 1000 km depth. Geophys. J. Int. 211 (3), 1628–1639.
Durand, S., Matas, J., Ford, S., Ricard, Y., Romanowicz, B., Montagner, J.-P., 2013. Insights from scs-s measurements on deep mantle attenuation. Earth Planet. Sci. Lett. 374, 101–110.
Durek, J., Ekstrom, G., 1996. A radial model of anelasticity consistent with long-period surface-wave attenuation. Bull. Seismol. Soc. Am. 86 (1A), 144–158.
Dziewonski, A., 1984. Mapping the lower mantle - determination of lateral heterogeneity in p-velocity up to degree and order-6. J. Geophys. Res., Solid Earth 89 (NB7), 5929.
Dziewonski, A., Anderson, D., 1981. Preliminary reference Earth model. Phys. Earth Planet. Inter. 25 (4), 297–356.
Ekstroem, G., Nettles, M., Dziewonski, A.M., 2012. The global cmt project 2004-2010: centroid-moment tensors for 13,017 earthquakes. Phys. Earth Planet. Inter. 200, 1–9.
Faul, U., Jackson, I., 2015. Transient creep and strain energy dissipation: an experimental perspective. Annu. Rev. Earth Planet. Sci. 43, 541–569.
Ford, S.R., Garnero, E.J., Thorne, M.S., 2012. Differential t* measurements via instantaneous frequency matching: observations of lower mantle shear attenuation heterogeneity beneath western Central America. Geophys. J. Int. 189 (1), 513–523.
French, S.W., Romanowicz, B.A., 2014. Whole-mantle radially anisotropic shear velocity structure from spectral-element waveform tomography. Geophys. J. Int. 199 (3), 1303–1327.
Hwang, Y.K., Ritsema, J., 2011. Radial $q_\mu$ structure of the lower mantle from teleseismic body-wave spectra. Earth Planet. Sci. Lett. 303 (3–4), 369–375.
Jenkins, J., Deuss, A., Cottaar, S., 2017. Converted phases from sharp 1000 km depth mid-mantle heterogeneity beneath western Europe. Earth Planet. Sci. Lett. 459, 196–207.
Kanamori, H., Anderson, D., 1977. Importance of physical dispersion in surface-wave and free oscillation problems - review. Rev. Geophys. 15 (1), 105–112.
Karato, S.-I., 2007. Microscopic Models for the Effects of Hydrogen on Physical and Chemical Properties of Earth Materials. Springer Netherlands, Dordrecht, pp. 321–356.
Kennett, B.L.N., Engdahl, E.R., 1991. Traveltimes for global earthquake location and phase identification. Geophys. J. Int. 105 (2), 429–465.
Kido, M., Čadek, O., 1997. Inferences of viscosity from the oceanic geoid: indication of a low viscosity zone below the 660-km discontinuity. Earth Planet. Sci. Lett. 151 (3–4), 125–137.
Komatitsch, D., Tromp, J., 2002a. Spectral-element simulations of global seismic wave propagation - I. Validation. Geophys. J. Int. 149 (2), 390–412.
Komatitsch, D., Tromp, J., 2002b. Spectral-element simulations of global seismic wave propagation - II. Three-dimensional models, oceans, rotation and self-gravitation. Geophys. J. Int. 150 (1), 303–318.
Laske, G., Masters, G., Ma, Z., Pasyanos, M., 2013. Update on crust1. 0—a 1-degree global model of Earth's crust. Geophys. Res. Abstr. 15, 2658.
Lawrence, J., Wysession, M., 2006. Qlm9:: a new radial quality factor ($q_\mu$) model for the lower mantle. Earth Planet. Sci. Lett. 241 (3–4), 962–971.
Lay, T., 2007. Deep Earth structure – lower mantle and D". In: Schubert, G. (Ed.), Seismology and the Structure of the Earth, vol. 1, pp. 619–654.
Lekić, V., Matas, J., Panning, M., Romanowicz, B., 2009. Measurement and implications of frequency dependence of attenuation. Earth Planet. Sci. Lett. 282 (1), 285–293.
Liu, C., Grand, S.P., 2018. Seismic attenuation in the African llsvp estimated from pcs phases. Earth Planet. Sci. Lett. 489, 8–16.
Mambole, A., Fleitout, L., 2002. Petrological layering induced by an endothermic phase transition in the Earth's mantle. Geophys. Res. Lett. 29 (22) 1–1–1–4.
Matheney, M., Nowack, R., 1995. Seismic attenuation values obtained from instantaneous-frequency matching and spectral ratios. Geophys. J. Int. 123 (1), 1–15.

Mattern, E., Matas, J., Ricard, Y., Bass, J., 2005. Lower mantle composition and temperature from mineral physics and thermodynamic modelling. Geophys. J. Int. 160 (3), 973–990.

Montagner, J.-P., Kennett, B.L.N., 1996. How to reconcile body-wave and normal-mode reference Earth models. Geophys. J. Int. 125 (1), 229–248.

Moulik, P., Ekstroem, G., 2014. An anisotropic shear velocity model of the Earth's mantle using normal modes, body waves, surface waves and long-period waveforms. Geophys. J. Int. 199 (3), 1713–1738.

Moulik, P., Ekstrom, G., 2025. Radial structure of the Earth: (ii) model features and interpretations. Phys. Earth Planet. Inter. 361.

Oki, S., Shearer, P.M., 2008. Mantle q structure from s-p differential attenuation measurements. J. Geophys. Res., Solid Earth 113 (B12).

Reid, F., Woodhouse, J., van Heijst, H., 2001. Upper mantle attenuation and velocity structure from measurements of differential s phases. Geophys. J. Int. 145 (3), 615–630.

Ricard, Y., Durand, S., Montagner, J.-P., Chambat, F., 2014. Is there seismic attenuation in the mantle? Earth Planet. Sci. Lett. 388, 257–264.

Ricard, Y., Richards, M., Lithgow-Bertelloni, C., Le Stunff, Y., 1993. A geodynamic model of mantle density heterogeneity. J. Geophys. Res., Solid Earth 98 (B12), 21895–21909.

Ritsema, J., Deuss, A., van Heijst, H.J., Woodhouse, J.H., 2011. S40rts: a degree-40 shear-velocity model for the mantle from new Rayleigh wave dispersion, teleseismic traveltime and normal-mode splitting function measurements. Geophys. J. Int. 184 (3), 1223–1236.

Romanowicz, B., Mitchell, B.J., 2007. Deep Earth structure -Q of the Earth from crust to core. In: Schubert, G. (Ed.), Seismology and the Structure of the Earth, vol. 1, pp. 731–774.

Ruan, Y., Zhou, Y., 2012. The effects of 3-d anelasticity (q) structure on surface wave amplitudes. Geophys. J. Int. 189 (2), 967–983.

Rudolph, M.L., Lekic, V., Lithgow-Bertelloni, C., 2015. Viscosity jump in Earth's mid-mantle. Science 350 (6266), 1349–1352.

Schubert, G., Anderson, C., Goldman, P., 1995. Mantle plume interaction with an endothermic phase-change. J. Geophys. Res., Solid Earth 100 (B5), 8245–8256.

Sipkin, S.A., Revenaugh, J., 1994. Regional variation of attenuation and travel time in China from analysis of multiple-scs phases. J. Geophys. Res., Solid Earth 99 (B2), 2687–2699.

Stixrude, L., Lithgow-Bertelloni, C., 2005. Thermodynamics of mantle minerals — I. Physical properties. Geophys. J. Int. 162 (2), 610–632.

Suetsugu, D., 2001. A low qscs anomaly near the south Pacific superswell. Geophys. Res. Lett. 28 (2), 391–394.

Sun, S., Zhou, Y., 2023. Age-independent oceanic plate thickness and asthenosphere melting from ss precursor imaging. J. Geophys. Res., Solid Earth 128 (2), e2022JB024805.

Talavera-Soza, S., Cobden, L., Faul, U.H., Deuss, A., 2025. Global 3d model of mantle attenuation using seismic normal modes. Nature 637 (8048).

Tarantola, A., Valette, B., 1982. Generalized non-linear inverse problems solved using the least-squares criterion. Rev. Geophys. 20 (2), 219–232.

Waszek, L., Schmerr, N.C., Ballmer, M.D., 2018. Global observations of reflectors in the mid-mantle with implications for mantle structure and dynamics. Nat. Commun. 9.

Weinstein, S., 1992. Induced compositional layering in a convecting fluid layer by an endothermic phase-transition. Earth Planet. Sci. Lett. 113 (1–2), 23–39.

Wessel, P., Smith, W.H., 1995. New version of the generic mapping tools. Eos Trans. AGU 76 (33), 329.

Widmer, R., Masters, G., Gilbert, F., 1991. Spherically symmetrical attenuation within the Earth from normal mode data. Geophys. J. Int. 104 (3), 541–553.

Zhang, B., Ni, S., Chen, Y., 2019. Seismic attenuation in the lower mantle beneath Northeast China constrained from short-period reflected core phases at short epicentral distances. Earth Planet. Phys. 3 (6), 537–546.

Zhang, Z., Irving, J.C.E., Simons, F.J., Alkhalifah, T., 2023. Seismic evidence for a 1000 km mantle discontinuity under the Pacific. Nat. Commun. 14 (1).

Zhou, Y., 2009. Surface-wave sensitivity to 3-d anelasticity. Geophys. J. Int. 178 (3), 1403–1410.

Zhu, M., Sun, S., Zhou, Y., Wu, Q., 2022. Mantle q structure from s, ss, sss and ssss amplitude measurements. Geophys. J. Int. 231 (1), 703–716.

Zindler, A., Hart, S., 1986. Chemical geodynamics. Annu. Rev. Earth Planet. Sci. 14, 493–571.